JOURNAL OF THERMOPHYSICS AND HEAT TRANSFER
Vol. 14, No. 3, July–September 2000

Cooling Mechanism of Expanding Plasmas Produced by Optical-Field-Induced Ionization

Shigeru Yonemura* and Kenichi Nanbu†
Tohoku University, Sendai 980-8577, Japan

Particle-in-cell simulation is carried out to investigate the cooling process of a multicharged dense plasma produced by optical-field-induced ionization. All coulomb collisions among charged particles are taken into consideration using Nanbu's theory of coulomb collisions and its recent extension to the case when the weight assigned to a simulated particle varies from particle to particle. The effect of coulomb collisions on the expanding plasma is very large. Two cases are considered: expansion of a source plasma 1) into a vacuum and 2) into an ambient cold plasma. The results obtained for the first case agree well with the self-similar hydrodynamic solution. In the second case, the rapid cooling of the multicharged plasma, which is essential for x-ray lasing, is accomplished. The mechanism of this cooling is clarified by the simulation. It is also shown that the expansion is accompanied by a dense wave front. Near the wave front, a double layer of electric charge is formed.

Nomenclature

c_s = ion acoustic speed
E = radial component of electric field
$\tilde{E}_j$ = electric field at $\tilde{r}_j$
e = electronic charge
f_j = charge assigned to grid point r_j
$\boldsymbol{g}$ = relative velocity
$\boldsymbol{h}$ = vector defined in Eq. (22)
J_∞ = total number of cells in the computational domain
k = Boltzmann's constant
$\ell n \Lambda$ = coulomb logarithm
m = mass of a particle
N = number of simulated particles in a cell at t equals 0
n = number density
Q_j = total charge assigned to grid point r_j
q = charge of a particle
R = radius of initial plasma core
R_∞ = radius of computational domain
r = radial position
r_j = radial position of jth grid point
$\tilde{r}_j$ = radial position of boundary between $(j-1)$th and jth cell
$s_{\alpha\beta}$ = parameter defined in Eq. (15)
T = temperature
t = time
U = uniform random number $(0 < U < 1)$
$\boldsymbol{v}$ = velocity
W = weight of a simulated particle
α, β = name of particle species
Δr = interval between adjacent grid points
Δt = time step
ϵ_0 = permittivity of free space
λ_D = electron debye length
μ = reduced mass
ρ = electric charge density
τ_p = period of electron plasma oscillation
χ = scattering angle

Subscripts

c = coulomb collision
e = electron
i = ion
r = r component
x, y, z = x, y, and z components
α, β = α, β species
$\alpha\beta$ = α–β collision
θ = θ component
0 = initial condition

I. Introduction

THE development of a tabletop x-ray laser system has been arousing worldwide interest because such a system is expected to result in innovations in biology, medical science, and microelectronics technology. For example, the spatial size of etched patterns in the most advanced technology will be reduced from micrometers to nanometers. Lithography technology using such an x-ray laser will enable 10-nm order processing, so that the production of terabit-order dynamic random access memory (DRAM) may become a reality.

In the initial stage of x-ray lasing, lasers with huge energy such as those used in nuclear fusion were employed as a light source to excite ions.[1,2] Various efforts have been made to reduce the energy of incident lasers and the size of x-ray laser systems.[3–5] One promising approach, which is called optical-field-inducedionization (OFI), has been proposed as a method of recombinationpumping.[6,7] OFI has several advantages compared with conventional recombination pumping. In the conventional scheme, first a multicharged high-temperatureplasma is produced by irradiation of a high-energy laser pulse onto a solid target. Next, the plasma is cooled by some cooling process such as adiabatic expansion to promote three-body recombinations, which generate a population inversion necessary for lasing. Note that the recombination cross section increases with the decrease of electron temperature. This is an indirect and expensive lasing process. By contrast, in OFI the optical field of an ultrashort, high-intensity laser pulse strips all electrons from atoms or ions directly by tunneling ionization.[8] The incident laser pulse for the OFI scheme requires intense peak power rather than large energy. Because of this, the cost of lasing can be reduced drastically, and frequently repetitive operations will become possible. Moreover, the temperature of the electrons produced by the OFI can be controlled by the polarization and wavelength of the incident laser. Hence, a relatively cold plasma can be produced by OFI, which is advantageous for recombination x-ray lasing.

The initial electron temperature of OFI plasmas, however, is still not low enough to provide a high rate of three-body recombination.

Received 8 November 1999; revision received 27 March 2000; accepted for publication 28 March 2000.

*Research Associate, Institute of Fluid Science; yonemura@ifs.tohoku.ac.jp.
†Professor, Institute of Fluid Science; nanbu@ifs.tohoku.ac.jp.

Therefore, some cooling process is necessary for OFI. Nagata et al.[9] proposed a modification of conventional OFI and reported the amplification of the Lyman-α transition at 13.5 nm in H-like Li ions. As a target medium, they employed a singly ionized lithium plasma in place of neutral gas used in conventional OFI. Their scheme provides some important advantages for the production of extremely cold electrons. In their experiments, the electron temperature measured was about 1.5 eV (Ref. 10). On the other hand, the average energy of the electrons produced by the laser irradiation was estimated to be 26 eV (Ref. 11). The mechanism of cooling after the irradiation has not yet been explained.

A reliable numerical modeling of lasing media is necessary to answer the questions posed in experiments. Some work based on the fluid model has been done on the simulation of lasing media.[12,13] Although plasmas are assumed to be in equilibrium in the fluid model, the electron energy distribution just after the irradiation of an ultrashort laser pulse largely deviates from the Maxwellian distribution.[14] Moreover, the rate of three-body recombinations occurring in x-ray lasing is largely affected by the degree of nonequilibrium in the electron energy distribution.[15] Therefore, the fluid model should be used with care. In contrast, the particle model makes sense for a large degree of nonequilibrium. Ditmire[16] calculated heating in the underdense plasma produced by OFI and examined the electron energy distribution by the use of a Monte Carlo simulation. Nanbu and Serikov[17] carried out a self-consistent particle-in-cell (PIC) simulation of expanding multicharged plasmas for x-ray laser sources. However, they did not consider the coulomb collisions, which will play an important role in a dense plasma. Recently, Nanbu[18] proposed an accurate theory of coulomb collisions for the Monte Carlo simulation. His theory was extended to the case when each species or each simulated particle has a different weight.[19]

The purpose of the present work is to examine the cooling process of the multicharged dense plasma generated by the irradiation of an ultrashort laser pulse by a self-consistent PIC simulation. We consider coulomb collisions using Nanbu's theory[18] and its extension.[19] In Sec. III, we revisit the problem treated in Ref. 17 and examine the effects of Coulomb collisions on the expanding plasma. The results obtained here are compared with a self-similar hydrodynamic solution for the expansion of a planar plasma into a vacuum.[20] In Sec. IV, we discuss the mechanism of the rapid cooling observed in the experiments.[9,10] We focus on the interaction between the source electrons produced by the OFI and the ambient cold electrons because the interaction plays a key role in the cooling process.

II. Numerical Method

A. Configuration

The computational domain is the inside of an infinitely long cylinder with a radius of $R_\infty = 100\,\mu$m. An ultrashort laser pulse is initially irradiated along the center axis of the computational domain. This results in the formation of a plasma core consisting of multicharged ions and high-temperature electrons. The time $t = 0$ is set at this moment. The initial plasma core is assumed to be an infinitely long cylinder with a radius of $R = 10\,\mu$m, which is coaxial with the computational domain. The initial plasma core is regarded as being surrounded by a vacuum in Sec. III and by an ambient cold plasma in Sec. IV. The plasma core and the ambient plasma are assumed to be spatially uniform and in different equilibria.

At $t = +0$, the plasma core is made free, and, hence, an expansion in the radial direction immediately takes place. All properties are assumed to depend only on r and t, which makes the problem spatially one dimensional.

B. PIC Simulation Method

In the PIC simulation, real particles are replaced by simulated particles whose number is much smaller than that of the real particles. A simulated particle represents W real particles, where W is the weight. The computational domain is divided into cells with the dimension of the electron debye length λ_D at $t = 0$. The simulation proceeds as follows.

1) At time $t = 0$, initial locations and velocities are given to simulated particles using their density and Maxwellian velocity distribution.

2) Radial distribution of charge density is calculated using the rule of charge assignment to grid points.[21] The electric field can be obtained from the resulting charge distribution.

3) New locations and velocities of simulated particles at the end of time step Δt are calculated by solving the equation of motion including the electric field, which is obtained in step 2.

4) Coulomb collisions in Δt are calculated.

5) Steps 2–4 are repeated to advance the time of a particle system up to a required time.

C. Grid Structure

We introduce two cell systems. One is a system to calculate the charge density and electric field and to sample macroscopic plasma parameters. The other is a system to calculate coulomb collisions. Each cell has the form of a ring. First, we explain the former cell system. We divide the computational domain ($r < R_\infty$) into equally spaced J_∞ intervals and call the radii $r_j = j\Delta r$, $j = 0, 1, \ldots, J_\infty$, grid points, where $\Delta r = R_\infty / J_\infty$. Let us regard a grid point as the center of a cell. We define the cell boundary by equal partitioning of the volume between two neighboring grid points. The radii $\tilde{r}_j$, $j = 1, 2, \ldots, J_\infty$, of cell boundaries are obtained from the volumetric relation

$$\pi\left(\tilde{r}_j^2 - r_{j-1}^2\right) = \pi\left(r_j^2 - \tilde{r}_j^2\right) \tag{1}$$

where it should be noted that $r_{j-1} < \tilde{r}_j < r_j$. Equation (1) yields

$$\tilde{r}_j = \sqrt{\left(r_j^2 + r_{j-1}^2\right)/2} \qquad (j = 1, 2, \ldots, J_\infty) \tag{2}$$

In the present simulation, the electric charges of simulated particles are assigned to the grid points r_j, whereas the electric field obtained from the charge distribution is calculated at the cell boundaries $\tilde{r}_j$.

Next we explain the second cell system with the boundaries r_0, $r_1, \ldots,$ for calculating coulomb collisions. Here we term the interval (r_{j-1}, r_j) collision cell j. The dimension of a collision cell is Δr, which is chosen to be nearly equal to the debye length λ_D. Coulomb forces between charged particles separated by more than a cell spacing λ_D are already considered in the electric field calculation in Sec. II.F. Therefore, we have only to consider coulomb collisions independently in each collision cell, disregarding collisions between two particles in different collision cells.

The electron debye length λ_D is

$$\lambda_D = \sqrt{\frac{\epsilon_0 k T_{e0}}{e^2 n_{e0}}} \tag{3}$$

where T_{e0} and n_{e0} are the electron temperature and number density in the initial plasma core, respectively.

D. Initial State of a Particle System

Here we use the cell system with the boundaries $r_0, r_1, \ldots$. The number of real particles in the cell between r_j and $r_j + \Delta r$ is approximately proportional to $2\pi r_j \Delta r$. This is small for small r_j; if we assign the same weight to all simulated particles, the number of simulated particles in a cell near the axis will become very small. This results in large statistical fluctuations of sampled data. If the number of simulated particles in a cell is nearly equal for all cells, the magnitude of the fluctuations will become much the same for all cells, which is advantageous. This notion results in the introduction of a smaller weight for a simulated particle in a cell nearer to the axis. Let N be the number of simulated particles in a cell at $t = 0$. The number N is set so as to be equal for all cells in the initial plasma core. Similarly, N is set so as to be equal for all cells in the initial ambient plasma. However, N for the ambient plasma is not always equal to that for the plasma core. Thus, the weight assigned to a simulated particle in the jth cell ($r_{j-1} < r < r_j$) is chosen as

$$W = \pi(2j - 1)(\Delta r)^2 L n_0 / N \tag{4}$$

where n_0 is the initial number density of real particles in the jth cell and $L(=\text{unity})$ is the axial length of the computational domain. Whether a particle moves from one cell to another or not, its initial weight is fixed at any time.

The initial location r_0 of a simulated particle in the jth cell is given by

$$r_0 = \Delta r\sqrt{(j-1)^2 + (2j-1)U} \tag{5}$$

where U is a uniform random number between 0 and 1; to reduce the fluctuation of r_0, we replace the random number U in Eq. (5) by $(i-0.5)/N$, where $i = 1, 2, \ldots, N$. The velocities of simulated electrons and simulated ions at $t = 0$ are sampled from the Maxwellian distribution for each species.

E. Charge Assignment

We employed the PIC assignment[21,22] using area weighting. Let us consider the one-dimensional r space. The charge qW of the real particles represented by one simulated particle, which is located between grid points r_j and r_{j+1}, is divided into the following fractions:

$$f_j = qW\frac{r_{j+1}^2 - r^2}{r_{j+1}^2 - r_j^2} \tag{6a}$$

$$f_{j+1} = qW\frac{r^2 - r_j^2}{r_{j+1}^2 - r_j^2} \tag{6b}$$

Then the fractional charges f_j and f_{j+1} are assigned to the grid points r_j and r_{j+1}, respectively. The total charge Q_j assigned to the point r_j can be obtained as the sum of f_j for all simulated electrons and ions located between r_{j-1} and r_{j+1}.

F. Electric Field

The electric field has only the radial component E. The Gauss law yields

$$E(r) = \frac{1}{2\pi r\epsilon_0}\int_V \rho\,\mathrm{d}V \tag{7}$$

where ρ is the charge density and V is the volume of the cylinder having the radius r and the unit axial length. By the substitution of the charge distribution Q_j obtained from the simulation into Eq. (7), the electric field $\tilde{E}_j[\equiv E(\tilde{r}_j)]$ at the cell boundary $\tilde{r}_j$ becomes

$$\tilde{E}_j = \frac{1}{2\pi\tilde{r}_j\epsilon_0}\sum_{j'=0}^{j-1} Q_{j'} \tag{8}$$

The electric field $E(r)$ at the position r of a simulated particle is interpolated from $\tilde{E}_j$ using the same rule as the charge assignment: if $\tilde{r}_{j-1} < r < \tilde{r}_j$, the electric field at r is given by

$$E(r) = \tilde{E}_{j-1}\cdot\frac{\tilde{r}_j^2 - r^2}{\tilde{r}_j^2 - \tilde{r}_{j-1}^2} + \tilde{E}_j\cdot\frac{r^2 - \tilde{r}_{j-1}^2}{\tilde{r}_j^2 - \tilde{r}_{j-1}^2} \tag{9}$$

For $r < \tilde{r}_1$,

$$E(r) = \tilde{E}_1\cdot\left(r^2\middle|\,\tilde{r}_1^2\right) \tag{10}$$

G. Particle Motion

Although the electric field is treated as one dimensional in the r direction, the particle motion is treated as three dimensional. The equation of motion is

$$m\frac{\mathrm{d}\boldsymbol{v}}{\mathrm{d}t} = q\boldsymbol{E} \tag{11}$$

where the vector $\boldsymbol{E}$ has only the radial component $E(r)$ given in Sec. II.F and m and $\boldsymbol{v}$ are the mass and velocity of a simulated particle, respectively. Because the Cartesian components of $\boldsymbol{v}$ are necessary in determining postcollisional velocities as is seen in Eqs. (20–22), we solve the equation of motion in the Cartesian system. Equation (11) is solved by means of the leap-frog scheme,[21] which relates the unknown velocity $\boldsymbol{v}^{l+(1/2)}$ at time $t = [l+\frac{1}{2}]\Delta t$ and position $\boldsymbol{r}^{l+1}$ at time $t = (l+1)\Delta t$ to those before one time step Δt:

$$\boldsymbol{v}^{l+\frac{1}{2}} = \boldsymbol{v}^{l-\frac{1}{2}} + (q/m)\boldsymbol{E}^l\,\Delta t \tag{12}$$

$$\boldsymbol{r}^{l+1} = \boldsymbol{r}^l + \boldsymbol{v}^{l+\frac{1}{2}}\Delta t \tag{13}$$

The time steps Δt_i for ions and Δt_e for electrons are set at $0.1\tau_p$ and $0.02\tau_p$, respectively, where τ_p is the period of electron plasma oscillation. It is

$$\tau_p = 2\pi\sqrt{\epsilon_0 m_e\big|\, e^2 n_{e0}} \tag{14}$$

where m_e is the electron mass. Usually, Δt_i is chosen to be nearly equal to τ_p in PIC simulations. In the present computational condition, however, ions move very fast, and we have found that Δt_i should be chosen to be much smaller than τ_p.

H. Treatment of Coulomb Collisions

The computational domain is divided into collision cells with the dimension $\Delta r(\simeq \lambda_D)$. Let us focus our attention on coulomb collisions in a collision cell. We consider electron–ion, electron–electron, and ion–ion collisions. Hereafter, the species is called α or $\beta(\neq\alpha)$. Our problem is how to determine the velocities of all simulated particles at the end of the time step Δt_c.

Nanbu's theory[18] is used in the simulation of coulomb collisions. A charged particle undergoes many successive small-angle collisions with ions and electrons during the time step Δt_c. In his theory, these small-angle collisions are grouped into a unique binary collision with a large scattering angle. Thanks to this feature of the theory, the computational task can be drastically reduced.

Collisions between unlike particles are called α–β collisions and collisions between like particles are called α–α or β–β collisions. Let the sets $\{\boldsymbol{v}_{\alpha i};\ i = 1, \ldots, N_\alpha\}$ and $\{\boldsymbol{v}_{\beta j};\ j = 1, \ldots, N_\beta\}$ be the velocities of simulated particles α and β at time t, respectively, where N_α and N_β are the numbers of simulated particles α and β in a cell. Let us call $\boldsymbol{v}_{\alpha i}$ the velocity of simulated particle α_i. Nanbu's theory[18] is summarized as follows. We focus our attention on a simulated particle α_i. The effects of α–β and α–α collisions on velocity $\boldsymbol{v}_{\alpha i}$ are assumed to be additive. First, we explain the treatment of α–β collisions in Δt_c. The postcollision velocity $\boldsymbol{v}'_{\alpha i}$ can be determined once the isotropy parameter

$$s_{\alpha\beta}(\Delta t_c) = \frac{\ell n\,\Lambda_{\alpha\beta}}{4\pi}\left(\frac{q_\alpha q_\beta}{\epsilon_0\mu_{\alpha\beta}}\right)^2 n_\beta g_{\alpha\beta}^{-3}\Delta t_c \tag{15}$$

is obtained, where q_α and q_β are the charges of particles α and β, $\mu_{\alpha\beta}$ is the reduced mass, n_β is the number density of species β, $g_{\alpha\beta}(=|\boldsymbol{v}_{\alpha i} - \boldsymbol{v}_\beta|)$ is the relative speed, and $\ell n\,\Lambda_{\alpha\beta}$ is the coulomb logarithm. The relative speed $g_{\alpha\beta}$ should be an average over $\boldsymbol{v}_\beta$ because a simulated particle α_i makes many small angle collisions in Δt_c. However, $g_{\alpha\beta}$ can be calculated by the use of a random sample of $\{\boldsymbol{v}_{\beta j};\ j = 1, \ldots, N_\beta\}$. $\Lambda_{\alpha\beta}$ is given by

$$\Lambda_{\alpha\beta} = \frac{2\pi\epsilon_0\lambda_D\mu_{\alpha\beta}\langle g_{\alpha\beta}^2\rangle}{|q_\alpha q_\beta|} \tag{16}$$

where $\langle\ \rangle$ denotes the expectation. We evaluate the mean square relative speed $\langle g_{\alpha\beta}^2\rangle$ by assuming that the velocity distributions of particles α and β are Maxwellian, so that $\langle g_{\alpha\beta}^2\rangle$ is given by

$$\langle g_{\alpha\beta}^2\rangle = (3kT_\alpha/m_\alpha) + (3kT_\beta/m_\beta) + (\langle\boldsymbol{v}_\alpha\rangle - \langle\boldsymbol{v}_\beta\rangle)^2 \tag{17}$$

where T and $\langle\boldsymbol{v}\rangle$ are the temperature and the flow velocity and subscripts α and β denote particles α and β, respectively.

The next step is to solve the nonlinear equation

$$\coth A - A^{-1} = \exp(-s_{\alpha\beta}) \tag{18}$$

and obtain the constant A that determines the probability density function for the scattering angle χ of a simulated particle α_i. A random sample of $\cos\chi$ is given by

$$\cos\chi = (1/A)\,\ell n(e^{-A} + 2U\sinh A) \tag{19}$$

where $0 < \chi < \pi$. The velocities $\boldsymbol{v}'_{\alpha i}$ and $\boldsymbol{v}'_{\beta j}$ after α_i–β_j collision are given by

$$\boldsymbol{v}'_{\alpha i} = \boldsymbol{v}_{\alpha i} - [m_\beta/(m_\alpha + m_\beta)][\boldsymbol{g}(1-\cos\chi) + \boldsymbol{h}\sin\chi] \tag{20}$$

$$\boldsymbol{v}'_{\beta j} = \boldsymbol{v}_{\beta j} + [m_\alpha/(m_\alpha + m_\beta)][\boldsymbol{g}(1-\cos\chi) + \boldsymbol{h}\sin\chi] \tag{21}$$

where m_α and m_β are the masses of particles α and β, $\boldsymbol{v}_{\beta j}$ is a random sample of $\{\boldsymbol{v}_{\beta j}; j = 1, \ldots, N_\beta\}$, $\boldsymbol{g}\,(=\boldsymbol{v}_{\alpha i} - \boldsymbol{v}_{\beta j})$ is the relative velocity, and the Cartesian components of the vector $\boldsymbol{h}$ are defined as

$$h_x = g_\perp\cos\varepsilon, \qquad h_y = -(g_y g_x\cos\varepsilon + g g_z\sin\varepsilon)/g_\perp$$
$$h_z = -(g_z g_x\cos\varepsilon - g g_y\sin\varepsilon)/g_\perp \tag{22}$$

where $g_\perp = (g_y^2 + g_z^2)^{1/2}$ and $\varepsilon = 2\pi U$.

The procedure for calculating α–α collisions is given simply by replacing β by α in Eqs. (15–21). The order of types of collision is not essential in the collision simulation, for example, we may first calculate all α–β collisions, next all α–α collisions, and last all β–β collisions.

Nanbu's theory[18] for coulomb collisions is extended to a general case when each species or each simulated particle has a different weight by Nanbu and Yonemura.[19] As mentioned in Sec. II.D, in the present simulation the weights of simulated particles differ from particle to particle; the weight is assigned at $t = 0$ and fixed at any time. The method of handling collisions between particles with different weights is described in detail in Ref. 19.

III. Effects of Coulomb Collisions

In this section, we treat the cylindrical expansion of a plasma core into a vacuum. We focus our attention on the effects of coulomb collisions on the expanding plasma because they are thought to play an important role in dense plasma. Furthermore, to verify the validity of our simulation code, we compare our simulation results with a self-similar hydrodynamic solution for the expansion of a planar plasma into a vacuum.[20]

A. Plasma Condition

It is assumed that at $t = 0$ the plasma core ($r < R$) is composed of only electrons and C^{5+} ions and that the region outside the core is a free space. The initial number densities and temperatures of the electrons and C^{5+} ions are chosen as

$$n_{e0} = 5n_{i0} = 5\times10^{25}\ \mathrm{m}^{-3} \tag{23}$$

$$kT_{e0} = kT_{i0} = 100\ \mathrm{eV} \tag{24}$$

where T_{i0} and n_{i0} represent the temperature and number density of the C^{5+} ions. For this condition, λ_D becomes 10.51 nm from Eq. (3). Therefore, we choose $\Delta r = 10$ nm and $J_\infty = 10{,}000$. We have $\tau_p = 1.575\times10^{-14}$ s from Eq. (14). The number of simulated particles per cell, N, is set at 4000 for both electrons and C^{5+} ions. The total number of simulated electrons (or ions) is $1000\times N$, where 1000 is the number of cells in the initial plasma core. We performed 12 simulations, each of which starts from an independent set of particle velocity data. All plasma properties are obtained by ensemble averaging of the 12 sets of data. The coulomb logarithm $\ell n\Lambda_{\alpha\beta}$ is assumed to be constant. We determine it from the initial condition, that is, $\ell n\Lambda_{ie} = 5.39$, $\ell n\Lambda_{ee} = 7.00$, and $\ell n\Lambda_{ii} = 3.78$. We chose the time steps for calculating i–e, e–e, and i–i collisions as $2\Delta t_{ie} = \Delta t_{ee} = \Delta t_{ii} = \tau_p$.

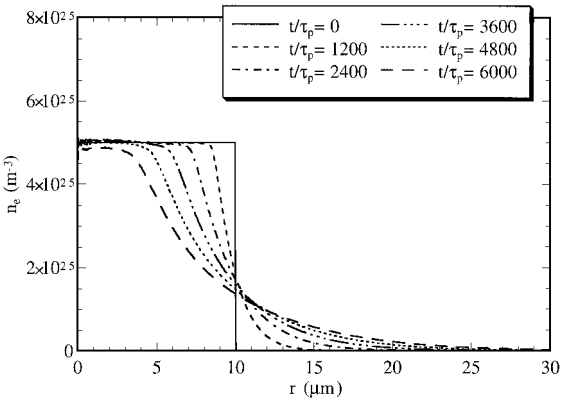

Fig. 1 Radial distributions of electron density.

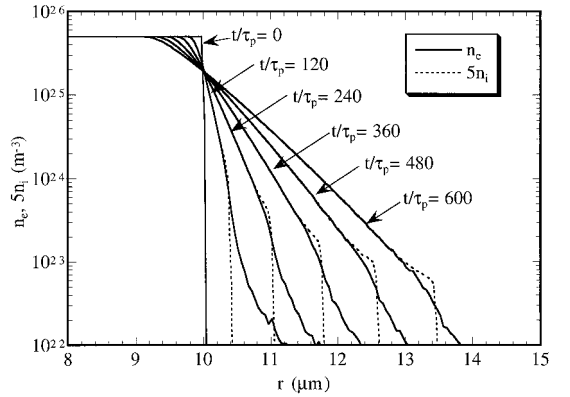

Fig. 2 Comparison of n_e and $5n_i$.

B. Results and Discussion

Figure 1 shows the time evolution of the electron number density n_e. The evolution of the ion number density n_i (not shown) is much like that of the electron number density. To examine the charge neutrality of the plasma, we show the comparison of n_e and $5n_i$ in Fig. 2 in the early stage of the expansion. In the expanding region, both densities decrease exponentially with radius r. Electrons in the forefront rush into a vacuum, and a rarefaction wave propagates backward into the plasma core. Except for the region near the ion front whose position is shown by the vertical dotted line, the overall expansion of the plasma can be regarded as an ambipolar phenomenon. The detailed behavior is as follows. Because electrons have much higher thermal velocities than ions, electrons are first apt to escape from the plasma, whereas positive ions are left behind. This results in induction of an electric field that pulls electrons inward and pushes ions outward. Consequently, the flow velocities of ions and electrons are adjusted by the field in such a way that the number fluxes of both species agree. We can divide Fig. 2 into three regions: the region near the ion front where charge neutrality is broken, the intermediate expanding region, and the innermost region still undisturbed by the rarefaction wave. We call the last region the plasma core. These features were discussed by Denavit.[20] He performed the PIC simulation to analyze the structure of one-dimensional planar expansion and confirmed that the particle simulation data correspond with a self-similar solution[23] obtained from the hydrodynamic model based on the assumptions of charge neutrality and isothermal electron equilibrium. Because the cylindrical expansion in the early stage can be regarded approximately as a planar expansion, we compare our simulation results with the self-similar hydrodynamic solution for a planar expansion in Fig. 3. The self-similar density profiles are given by

$$n_i = n_{i0}\exp\{-[1 + (1/c_s)\cdot(r - R)/t]\} \tag{25}$$

where $c_s = \sqrt{(ZkT_{e0}/m_i)} = 6.338\times10^4$ m/s is the ion acoustic speed, $Z(=5$ for $C^{5+})$ is the charge of ion in units of electronic

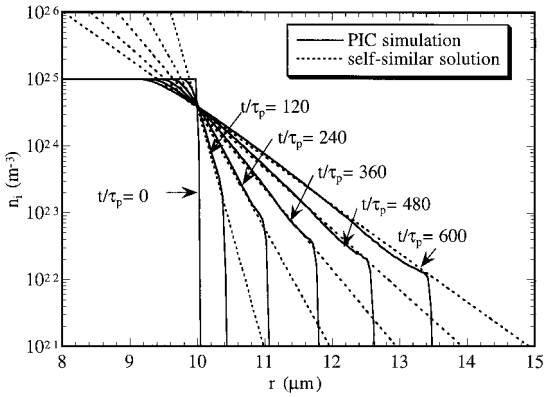

Fig. 3 Simulated ion density and self-similar solution.

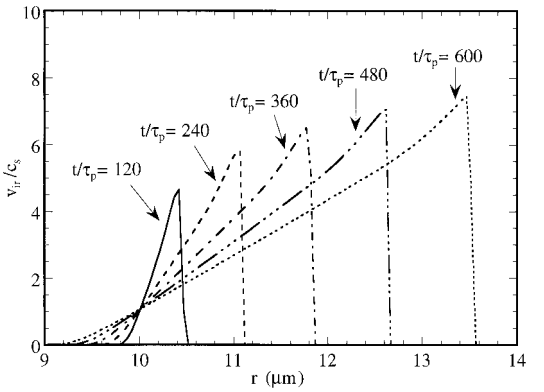

Fig. 4 Evolution of ion radial flow velocity.

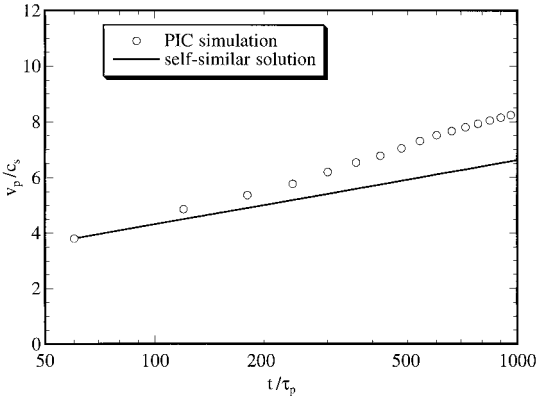

Fig. 5 Simulated ion front velocity and self-similar solution.

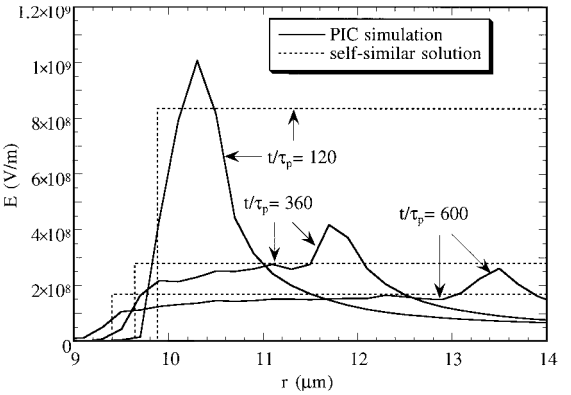

Fig. 6 Simulated electric field and self-similar solution.

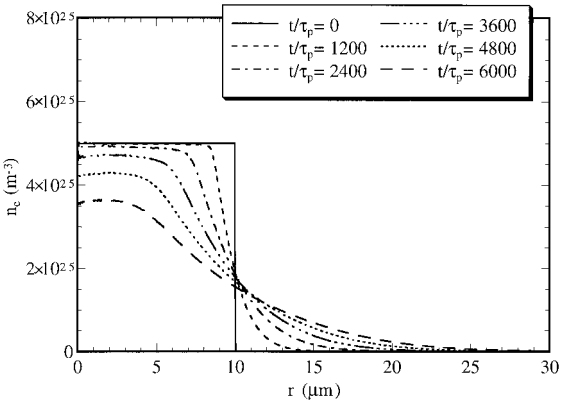

Fig. 7 Electron density without coulomb collisions.

charge e, and m_i is the ion mass. The ion density profiles obtained from the present simulation correspond very well with the self-similar solution up to the ion front.

The ion radial flow velocity v_{ir} normalized by the ion acoustic speed c_s is shown in Fig. 4, where the vertical lines indicate the ion front. The speed of the ion front increases and reaches a point 10 times as high as the ion acoustic speed for $t \geq 4000\tau_p = 6.3 \times 10^{-11}$ s (not shown). The linear increase of the ion flow velocity in Fig. 4 was predicted by Denavit.[20] This velocity profile is quite similar to that behind a blast wave.[24] All curves intersect at $r = 10\,\mu$m; the flow velocity at the edge of the initial plasma core ($r = 10\,\mu$m) remains constant ($v_{ir} \simeq c_s$). This corresponds to the self-similar solution.[20] Furthermore, in the self-similar solution, a group of ions that are initially located near the edge of the plasma core and have the flow velocity v_1 at an early time t_1 are accelerated according to

$$v_p = c_s \ln(t/t_1) + v_1 \tag{26}$$

The peak velocities v_p in Fig. 4, which is the velocity of the ion front, represent the flow velocity of such ions. The velocities v_p obtained from the PIC simulation are compared in Fig. 5 with Eq. (26), where $t_1 = 9.450 \times 10^{-13}$ s ($= 60\tau_p$) and $v_1 = 2.410 \times 10^5$ m/s. The simulation results show a qualitative agreement with the self-similar solution. The reason for the deviation from the self-similar solution can be explained by considering the electric field. The calculated electric field is compared with the self-similar solution in Fig. 6. The calculated field inside the peak agrees approximately with the self-similar solution, $E = kT_{e0}/ec_s t$. Because the peak is located at the same position as the ion front, the ions near the front are accelerated more than the case of the self-similar solution.

Plasmas for x-ray laser sources are so dense that coulomb collisions are expected to have significant effects on the expanding flow. To examine these effects, we performed simulations with and without coulomb collisions. Figure 7 shows the time evolution of the electron density in the case when coulomb collisions are disregarded. Compare Fig. 7 with Fig. 1. In Fig. 1 the density of the plasma core remains constant until the rarefaction wave arrives. This is because coulomb collisions prevent the electrons in the plasma core from escaping outward.

Figure 8 shows the radial distributions of the electron temperatures in the case when coulomb collisions are considered, where T_{er}, $T_{e\theta}$, and T_{ez} are the radial, azimuthal, and axial components, respectively. The vertical lines in Fig. 8 represent the location at which the electron density is 1% of n_{e0}. Beyond these lines, the meaningful electron temperature cannot be sampled because of large fluctuations. Temperature components hardly vary over the region from the center of the plasma core to the vertical line. To be precise, the temperature shows a slight decrease with radius r. Note that the edge of the undisturbed plasma core seen in Fig. 1 cannot be recognized in Fig. 8 and that all temperature components agree well. These features are quite different from the case for no coulomb collision. In the case of no coulomb collision, the electron temperature (not shown) varies largely with r, and the temperature profile

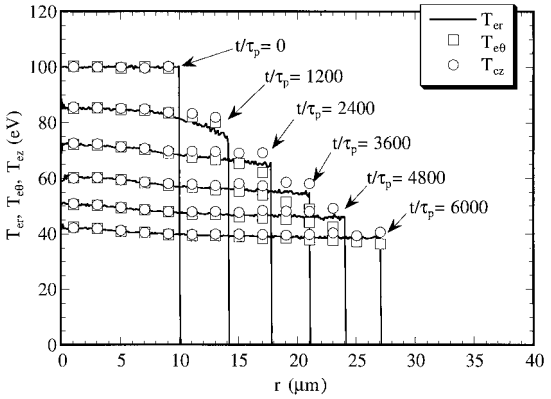

Fig. 8 Radial distributions of electron temperature components.

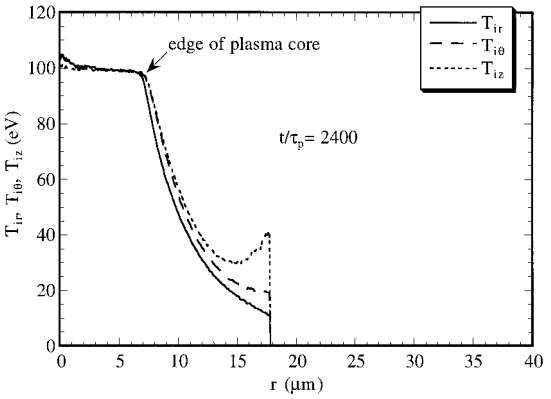

Fig. 9 Radial distributions of ion temperature components.

is snapped at the edge of the plasma core. Furthermore, without coulomb collisions, a large separation appears among the temperature components. Coulomb collisions make the separation very small. Because electrons move rapidly from cell to cell, the spatial nonuniformity of the electron temperature is greatly reduced, as is shown in Fig. 8, whereas the ion temperature in Fig. 9 shows a large spatial variation. Figure 8 also shows that the electron temperature components decrease with time. The electron cooling in Fig. 8 is not due to adiabatic expansion, but rather to the conversion of the electron thermal energy to the energy of a directed flow.

Figure 9 shows the ion temperature components for the case when coulomb collisions are considered, where T_{ir}, $T_{i\theta}$, and T_{iz} are the radial, azimuthal, and axial components, respectively. In Fig. 9, the separation among the temperature components, which is large without coulomb collisions, becomes very small. Coulomb collisions among ions greatly reduce the temperature separation, as in the case of electrons. Different from the electron temperature shown in Fig. 8, we can clearly recognize the edge of the plasma core in Fig. 9. Because ions move much more slowly than electrons, the spatial nonuniformity of ion temperature is kept in the expansion. No ion cooling occurs in the plasma core.

IV. Rapid Cooling Accomplished by an Ambient Cold Plasma

As described in the Introduction, the rapid cooling of the OFI plasma is essential for increasing the rate of three-body recombinations. Nagata et al.[9] succeeded in cooling an OFI plasma using a singly ionized lithium plasma as a target medium, whereas neutral gas is used as the target in the conventional OFI, and he demonstrated the amplification of the Lyman-α transition at 13.5 nm in H-like Li ions. However, this cooling mechanism has not yet been explained. In Sec. IV, we try to clarify the cooling mechanism by a PIC simulation.

A. Plasma Condition

At $t = 0$ the plasma core ($r < R$), which is produced by the OFI along the axis, is composed of electrons and Li^{3+} ions. The core is surrounded by a cold plasma composed of electrons and Li^{+} ions. In the initial plasma core, the temperatures of the electrons and Li^{3+} ions are set at 100 eV, and the number densities of the electrons and Li^{3+} ions are set at 3×10^{24} m^{-3} and 10^{24} m^{-3}, respectively. In the ambient plasma, the temperatures of the electrons and Li^{+} ions are set at 1 eV, and the number densities of the electrons and Li^{+} ions are set at 10^{24} m^{-3}. In this condition, λ_D is 42.92 nm from Eq. (3) and τ_p is 6.430×10^{-14} s from Eq. (14). Because the cell dimension Δr should be of the order of λ_D, we choose $\Delta r = 40$ nm and $J_\infty = 2500$. N is set at 3000 for both the electrons and Li^{3+} ions in the initial plasma core, whereas N is set at 1000 for both the electrons and Li^{+} ions in the initial ambient plasma. The number of cells in the initial plasma core is 250 and that in the initial ambient plasma is 2250. Therefore, the numbers of simulated electrons, simulated Li^{3+} ions, and simulated Li^{+} ions are 3×10^6, 7.5×10^5, and 2.25×10^6, respectively. We performed 15 simulations, each of which starts from an independent data set. All plasma properties are obtained by ensemble averaging of the 15 sets of data. We choose the time step for calculating coulomb collisions to be τ_p. The coulomb logarithm $\ell n \Lambda_{\alpha\beta}$ is calculated from Eqs. (16) and (17) at each collision time step in each cell.

B. Results and Discussion

Figure 10 shows the evolution of the electron number density n_e. With time, a dense wave front expands in the radial direction, while the electron density near the center axis decreases. The density of the expanding wave front decreases with time. It is interesting that the electron number density near the center axis becomes lower than that of the ambient plasma for $t \geq 3600\tau_p$. This results in the formation of a crater in the electron density profile at the back of the moving wave front.

Figure 11 shows the relation among the number densities of the electrons, Li^{3+} ions, and Li^{+} ions. We have found that the charge

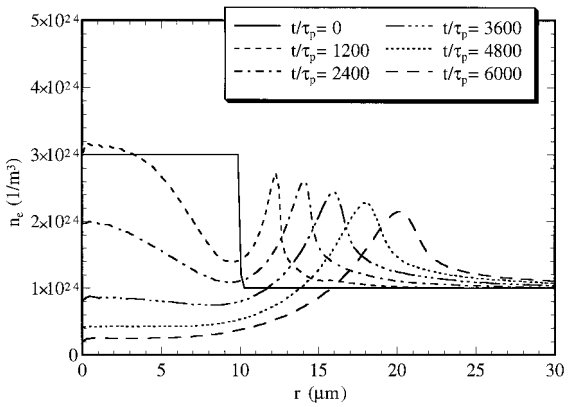

Fig. 10 Radial distributions of electron density.

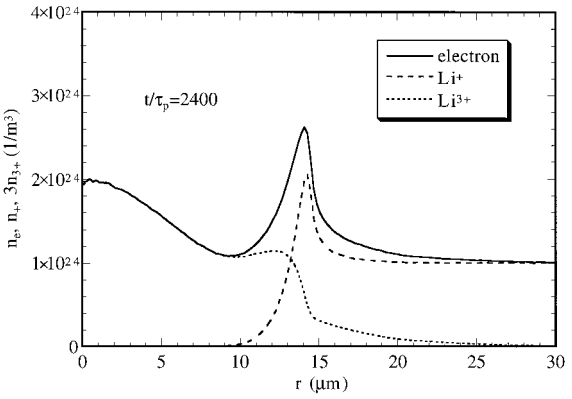

Fig. 11 Relation among n_e, $3n_{3+}$ and n_+.

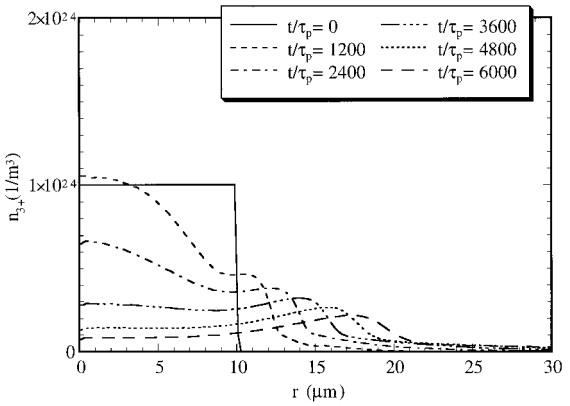

Fig. 12 Radial distributions of Li^{3+} density.

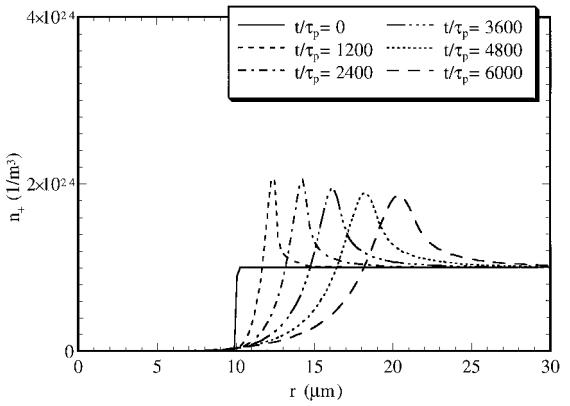

Fig. 13 Radial distributions of Li^{+} density.

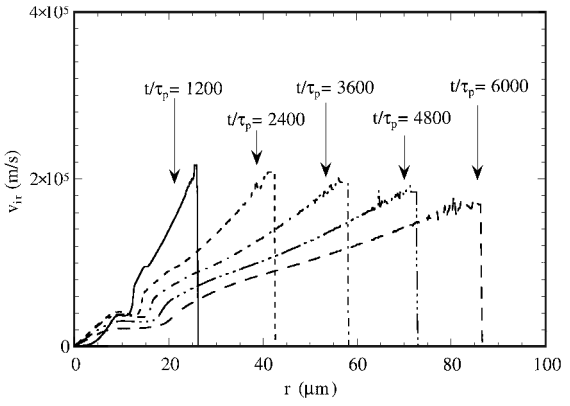

Fig. 14 Evolution of Li^{3+} radial velocity.

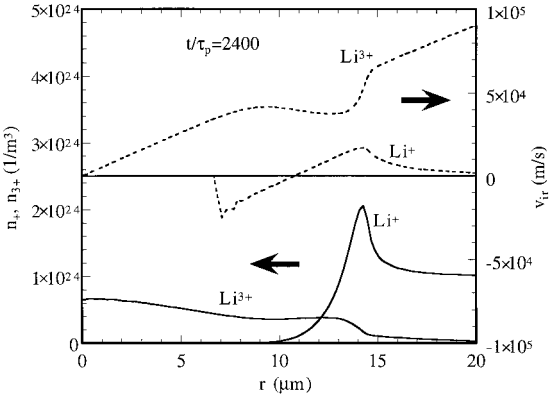

Fig. 15 Relation between velocities and densities of Li^{3+} and Li^{+}.

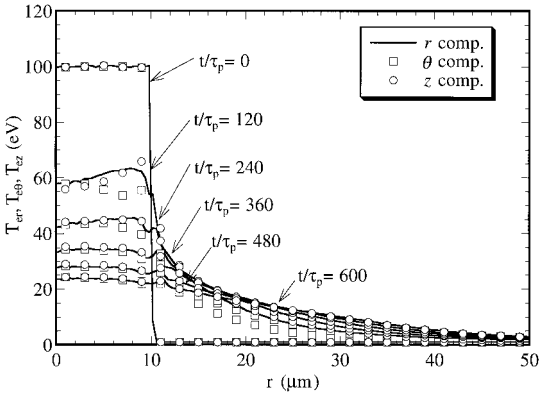

Fig. 16 Radial distributions of electron temperature components.

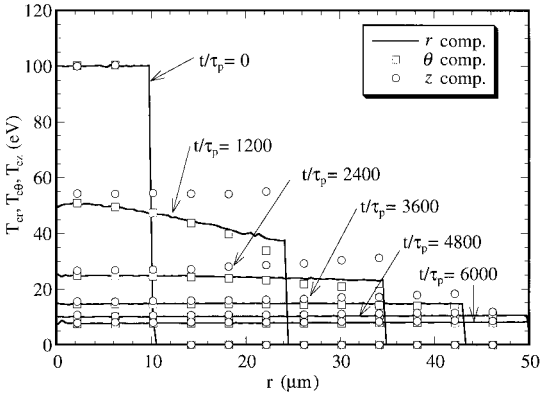

Fig. 17 Electron temperature components for the case of expansion into a vacuum.

neutrality of the plasma is almost maintained: n_e is approximately equal to the sum of $3n_{3+}$ and n_+, where n_{3+} and n_+ are the number densities of Li^{3+} ions and Li^{+} ions, respectively. The reason why the dense wave front is formed can be understood from Figs. 12 and 13, which show the spatiotemporal evolution of the Li^{3+} density and Li^{+} density, respectively. Because the Li^{3+} flow pushes the Li^{+} flow forward, the Li^{+} density increases in the region of impingement. Because the masses of both ion species are much larger than the electron mass, the density profile of electrons is settled in such a way as to maintain the charge neutrality. Namely, the distribution of positive charge formed by impinging ion flows results in the dense wave front in the electron density profile.

Figure 14 shows the evolution of the radial flow velocity v_{ir} of Li^{3+}. We can see that the ion front runs in the radial direction and that its speed decreases with time. The ions near the front lose their speed due to braking by the ambient plasma. Furthermore, although the ion velocity showed a linear increase with r in the case of no ambient plasma (Fig. 4), a dent now appears in the ion velocity profile. The cause of the dent can be understood from Fig. 15, which shows the number densities and flow velocities of Li^{3+} and Li^{+}. Because the Li^{3+} flow impinges on the denser Li^{+} flow, the Li^{3+} flow velocity is suppressed near the peak of n_+.

Figure 16 shows the distribution of the electron temperature. The electron temperature in the core region decreases by 40% in a brief period of $120\tau_p$ ($=7.72\times10^{-12}$ s). For $t \geq 480\tau_p$, the electron temperature shows a monotonic decrease in the radial direction. There is no appreciable separation among the temperature components. To examine the effects of the ambient plasma, the PIC simulation of Li^{3+} plasma is also performed for the case in which the initial plasma core is surrounded by a vacuum. Figure 17 shows the electron temperature components in the case of a vacuum. The electron temperature decreases about 10 times as slowly as it does in the case when the ambient plasma exists. From these results, it is found that

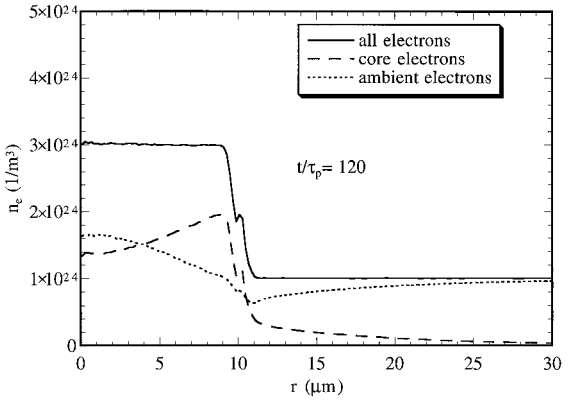

Fig. 18 Mixing of electrons from core plasma and ambient plasma.

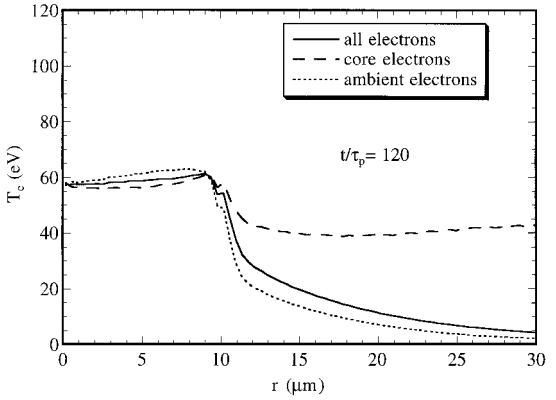

Fig. 19 Electron temperatures for all electrons, core electrons, and ambient electrons.

an ambient cold plasma makes a great contribution to the cooling of an OFI plasma. Next, let us focus on the mechanism of this cooling.

First we divide electrons into two groups. One is the group of the electrons that are initially in the plasma core, and the other is the group of the electrons initially included in the ambient plasma. Figure 18 shows the number densities of the two groups in the early stage of expansion ($t = 120\tau_p$). We can see that the mixing of the two groups proceeds much more quickly than the expansion itself. At $t = 120\tau_p$, the electrons coming from the background amount to about a half of the total number of electrons in the plasma core. This is the reason why the electron temperature in the core region decreases so fast. Figure 19 shows the temperatures of the two groups. Note that the temperature profiles of both groups coincide very well in the core region. Energy transfer between the two groups due to coulomb collisions is very effective.

The next question is why the mixing of the two electron groups proceeds so quickly. Figure 20 shows the distribution function for the radial velocity of electrons existing near the edge of the plasma core at $t = 60\tau_p = 3.86 \times 10^{-12}$ s. The velocity distribution of the bold line has two peaks. It is far from Maxwellian. Electrons from the background flow inward, while electrons from the core flow outward. This feature of electrons results in two peaks in the velocity distribution. The reason why electrons behave in such a way can be explained from Fig. 21, which shows the electric field and charge density near the edge of the plasma core at $t = 60\tau_p$. At $t = +0$, electrons with high energy near the edge of the plasma core start to escape from the core and ions near the edge are left as they stand because electrons move much more quickly than ions. Such positive ions induce an intense electric field near the edge, as shown in Fig. 21. This electric field pulls electrons inward. However, the electrons pulled into the plasma core are not the electrons that escaped from the core but the electrons with low energy in the background. This is the mechanism of the rapid mixing of the electron groups. In other words, this is the mechanism of the rapid cooling observed in the Nagata et al. experiments.[9,10]

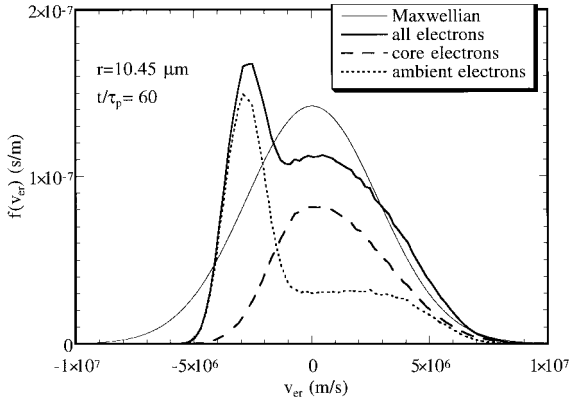

Fig. 20 Distribution of radial velocity of electrons near the edge of plasma core.

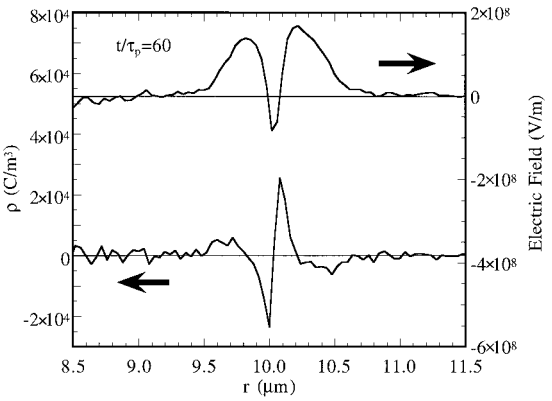

Fig. 21 Electric field and charge density near the edge of plasma core.

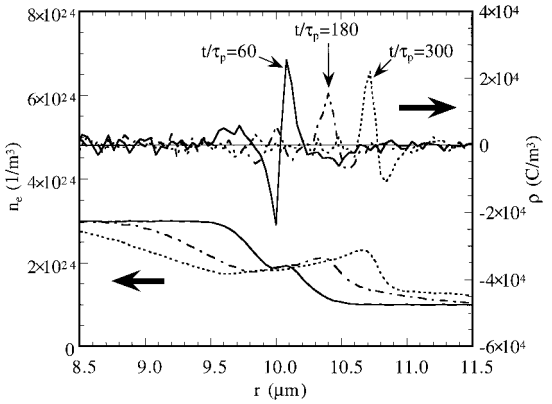

Fig. 22 Evolution of double layer of electric charge and electron density.

Furthermore, we can recognize a double layer of electric charge in Fig. 21. Figure 22 shows the time evolution of the double layer. It can be seen that a double layer always appears at the dense wave front.

V. Conclusion

We developed a PIC simulation code including the latest coulomb collision algorithm. Using this code, the mechanism of cooling in OFI plasma was clarified. The results obtained can be summarized as follows. Items 1 and 2 are relevant to the expansion of C^{5+} plasma into a vacuum, and other items are pertinent to the expansion of high-temperature Li^{3+} plasma into an ambient cold Li^{+} plasma.

1) In the case when the initial plasma core expands into a free space, the ion density obtained from the PIC simulation agrees well with a self-similar hydrodynamic solution.

2) The effect of coulomb collisions on the expansion is large: Coulomb collisions greatly recover the translational equilibrium of electrons and ions, largely reducing the separation of temperature components during the expansion.

3) Expansion of the plasma proceeds, accompanied by a dense wave front. The electron density behind the wave front decreases with time, and in the later stage of expansion, this electron density becomes lower than that of the ambient plasma.

4) The radial distribution of the electron density can be explained by the impingement of the Li^{3+} flow and Li^{+} flow. The Li^{3+} flow pushes the Li^{+} flow forward, and hence, the Li^{+} density profile shows a peak in the location of impingement, where the electron density profile also shows a peak because of charge neutrality.

5) The electron temperature in the core region drops very quickly. This is ascribable to a rapid invasion of the ambient cold electrons into the core.

6) A double layer is formed in the wave front; charge density changes signs in the layer. The electric field corresponding to the double layer pulls electrons inward. The electrons pulled into the core are mostly the electrons with low energy coming from the background, which is the reason for the rapid invasion described in item 5.

7) A large nonequilibrium in the velocity distribution function shows that only the particle model makes sense in such problems as are treated in this work.

Acknowledgments

This work was supported by the Japan Atomic Energy Research Institute (Kansai Research Establishment) as a part of Advanced Laser System Research. S. Yonemura, one of the authors, was supported by the Grant-in-Aid for Encouragement of Young Scientists (Grant 10750116). The numerical simulations were carried out using the supercomputer Cray C916 at the Institute of Fluid Science, Tohoku University. We would like to express our thanks to A. Sasaki of the Japan Atomic Energy Research Institute and V. V. Serikov of Nippon Sheet Glass for their valuable advice on the present study.

References

[1]Matthews, D. L., Hagelstein, P. L., Rosen, M. D., Eckart, M. J., Ceglio, N. M., Hazi, A. U., Medecki, H., MacGowan, B. J., Trebes, J. E., Whitten, B. L., Campbell, E. M., Hatcher, C. W., Hawryluk, A. M., Kauffman, R. L., Pleasance, L. D., Rambach, G., Scofield, J. H., Stone, G., and Weaver, T. A., "Demonstration of a Soft X-Ray Amplifier," *Physical Review Letters*, Vol. 54, No. 2, 1985, pp. 110–113.

[2]Suckewer, S., Skinner, C. H., Milchberg, H., Keane, C., and Voorhees, D., "Amplification of Stimulated Soft-X-Ray Emission in a Confined Plasma Column," *Physical Review Letters*, Vol. 55, No. 17, 1985, pp. 1753–1756.

[3]Hara, T., Ando, K., Kusakabe, N., Yashiro, H., and Aoyagi, Y., "Soft X-Ray Lasing in an Al Plasma Produced by a 6 J Laser," *Japanese Journal of Applied Physics*, Vol. 28, No. 6, 1989, pp. L1010–L1012.

[4]Kim, D., Skinner, C. H., Umesh, G., and Suckewer, S., "Gain Measurements at 18.22 nm in C VI Generated by a Nd:Glass Laser," *Optics Letters*, Vol. 14, No. 13, 1989, pp. 665–667.

[5]Basu, S., Hagelstein, P. L., Goodberlet, J. G., Muendel, M. H., and Kaushik, S., "Amplification in Ni-Like Nb at 204.2 Å Pumped by a Table-Top Laser," *Applied Physics B*, Vol. 57, 1993, pp. 303–307.

[6]Burnett, N. H., and Corkum, P. B., "Cold-Plasma Production for Recombination Extreme-Ultraviolet Lasers by Optical-Field-Induced Ionization," *Journal of the Optical Society of America B*, Vol. 6, No. 6, 1989, pp. 1195–1199.

[7]Eder, D. C., Amendt, P., DaSilva, L. B., London, R. A., MacGowan, B. J., Matthews, D. L., Penetrante, B. M., Rosen, M. D., Wilks, S. C., Donnelly, T. D., Falcone, R. W., and Strobel, G. L., "Tabletop X-Ray Lasers," *Physics of Plasmas*, Vol. 1, No. 5, 1994, pp. 1744–1752.

[8]Augst, S., Strickland, D., Meyerhofer, D. D., Chin, S. L., and Eberly, J. H., "Tunneling Ionization of Noble Gases in a High-Intensity Laser Field," *Physical Review Letters*, Vol. 63, No. 20, 1989, pp. 2212–2215.

[9]Nagata, Y., Midorikawa, K., Kubodera, S., Obara, M., Tashiro, H., and Toyoda, K., "Soft-X-Ray Amplification of the Lyman-α Transition by Optical-Field-Induced Ionization," *Physical Review Letters*, Vol. 71, No. 23, 1993, pp. 3774–3777.

[10]Nagata, Y., Midorikawa, K., Kubodera, S., Obara, M., Tashiro, H., Toyoda, K., and Kato, Y., "Production of an Extremely Cold Plasma by Optical-Field-Induced Ionization," *Physical Review A*, Vol. 51, No. 2, 1995, pp. 1415–1419.

[11]Midorikawa, K., Nagata, Y., Kubodera, S., Obara, M., and Toyoda, K., "An Optical Field-Induced Ionization X-Ray Laser Using a Preformed Plasma Scheme," *IEEE Journal of Selected Topics in Quantum Electronics*, Vol. 1, No. 3, 1995, pp. 931–940.

[12]Sasaki, A., Yoneda, H., Ueda, K., and Takuma, H., "2-Dimensional Hydrodynamics, Atomic Kinetics, and Line Transfer Simulation for Recombination Pumped Soft X-Ray Lasers," *Journal of Quantitative Spectroscopy and Radiative Transfer*, Vol. 54, No. 1/2, 1995, pp. 353–360.

[13]Kim, N. S., Djaoui, A., Key, M. H., Neely, D., Preston, S. G., Zepf, M., Smith, C. G., Wark, J. S., Zhang, J., and Offenberger, A. A., "Extreme Ultraviolet Line Emission at 24.7 nm from Li-Like Nitrogen Plasma Produced by a Short KrF Excimer Laser Pulse," *Applied Physics Letters*, Vol. 69, No. 7, 1996, pp. 884–886.

[14]Mohideen, U., Sher, M. H., Tom, H. W. K., Aumiller, G. D., Wood, O. R., II, Freeman, R. R., Bokor, J., and Bucksbaum, P. H., "High Intensity Above-Threshold Ionization of He," *Physical Review Letters*, Vol. 71, No. 4, 1993, pp. 509–512.

[15]Nanbu, K., Yonemura, S., and Sasaki, A., "Particle Modeling of Ionization and Three-Body Recombination in Fully Ionized Plasmas," *Japanese Journal of Applied Physics*, Vol. 38, Pt. 1, No. 7B, 1999, pp. 4460–4464.

[16]Ditmire, T., "Simulations of Heating and Electron Energy Distributions in Optical Field Ionized Plasmas," *Physical Review E*, Vol. 54, No. 6, 1996, pp. 6735–6740.

[17]Nanbu, K., and Serikov, V. V., "Particle-in-Cell Simulation of Expansions of Dense Plasma Sources for X-Ray Laser Systems," *Japanese Journal of Applied Physics*, Vol. 36, Pt. 1, No. 7A, 1997, pp. 4497–4508.

[18]Nanbu, K., "Theory of Cumulative Small-Angle Collisions in Plasmas," *Physical Review E*, Vol. 55, No. 4, 1997, pp. 4642–4652.

[19]Nanbu, K., and Yonemura, S., "Weighted Particles in Coulomb Collision Simulations Based on the Theory of a Cumulative Scattering Angle," *Journal of Computational Physics*, Vol. 145, No. 2, 1998, pp. 639–654.

[20]Denavit, J., "Collisionless Plasma Expansion into a Vacuum," *Physics of Fluids*, Vol. 22, No. 7, 1979, pp. 1384–1392.

[21]Birdsall, C. K., and Langdon, A. B., *Plasma Physics via Computer Simulation*, McGraw–Hill, New York, 1985, Chaps. 2, 14.

[22]Hockney, R. W., and Eastwood, J. W., *Computer Simulation Using Particles*, IOP Publishing, Bristol, England, U.K., 1988, Chap. 5.

[23]Allen, J. E., and Andrews, J. G., "A Note on Ion Rarefaction Waves," *Journal of Plasma Physics*, Vol. 4, Pt. 1, 1970, pp. 187–194.

[24]Howarth, L., *Modern Developments in Fluid Dynamics: High Speed Flow*, Vol. 1, Clarendon, Oxford, 1953, Chap. 4, p. 156.